Exoplanets A: Lab assignment

L. Welzel [s3079449][1]

Leiden University,
e-mail: welzel@strw.leidenuniv.nl

Submitted May 18, 2023

1. Introduction

This study aims to investigate the evolution, mass-radius relationships, stability, and temperature-pressure profiles of sub-Neptune exoplanets from simulations.

Understanding the evolution of sub-Neptunes enhances our ability to predict the characteristics of undiscovered exoplanets, refine our understanding of their interiors, and improve our models of planetary formation and evolution. Additionally, understanding the physics of sub-Neptunes can potentially reveal information about the conditions in our own solar backyard where the interior of Neptune and Uranus are laboratories for physics and chemistry at extreme conditions which are impossible to create on earth.

In section 2 we describe the simulation and postprocessing pipeline, after which we show and interpret our results in section 3. section 4 contains a short discussion of our findings and perspectives for future work.

2. Method

We run Modules for Experiments in Stellar Astrophysics (MESA Paxton et al. 2011, 2013, 2015, 2018, 2019; Jermyn et al. 2023) to simulate the evolution of a population of planets with core mass M_{core} between 1.2 and 25 $M_\oplus$ and envelope mass fraction f between 0.001 and 0.2.[1] We run both a grid search (GS, 126 samples) and random search (RS, 200 samples) over this parameter space and sample M_{core} and f uniformly and log-uniformly respectively. The experiment data is reported in section A.3.3. We first set-up a planet with placeholder parameters and then repeatedly tweak-evolve the planet until it fits the desired parameters after which the planet is free to evolve for 5 Gyr.

Our planets are H/He dominated and we assume its core composition is that of Earth, Equation 1. The total planet mass M_P is a function of the two main parameters, Equation 2. We assume that the initial internal mean entropy is $S = 9kB$/baryon and inflate the planet with an artificial internal luminosity (2×10^{27} $ergs/s$) until the entropy target is reached after we adjust the internal luminosity to match the assumed core regeneration

rate of 5×10^{-8} $erg/g/s$.

$$\frac{R}{R_\oplus} = \left(\frac{M}{M_\oplus}\right)^{0.27} \tag{1}$$

$$M_P = \frac{M_{core}}{1-f} \begin{cases} M_p = M_{core} + M_{env} \\ f_{env} = \frac{M_{env}}{M_p} \end{cases} , \tag{2}$$

where we note that the planet mass is dissimilar for each of the the planets in the assignment (Miguel et al. (2023b), hereafter ExoP-Lab), see also Figure 3. We use modified `mesa_runner.py`, `inlist_editor.py`, and `star_job` defaults to automate the survey. Furthermore, we built our own post-processing pipeline[2] using `pandas`, `numpy`, `h5py`, and `pathos` to parallelize the data reduction pipeline by Welzel et al. (2021)[3]. We do not parallelize the experiments since MESA is internally multi-threaded.

3. Results

We run more experiments over a larger space than required by ExoP-Lab, however we report only results from the required planets in the main text for clarity and report any additional results in section A.3.2.

3.1. Radius Evolution

The evolution of the radius of the simulated planets is shown in Figure 1. The planets shrink over time, balancing their gravitational and radiated energy through the Kelvin-Helmholtz contraction, see Equation 3. As the planet contracts this mechanism becomes less efficient and the timescale for further contraction increases. This leads to asymptotic contraction as degeneracy in the core of the planet increases. Furthermore, the (nonphysical) constant artificial internal luminosity we use to simulate internal energy production increases the final equilibrium radius further. Planets with larger envelopes are more extended as the density in the envelope is lower compared to the interior. Still, planets with large envelopes contract more quickly since they are less stable against further compression, again as a consequence of the lower envelope density. Furthermore, radiative heat loss is

---

[1] We only report successful experiments. Some parameterizations (large envelope mass fraction and core mass) violate MESA constraints and terminate prematurely. This is expected behaviour, see also section A.3.1.

[2] See https://gitlab.com/lukas_welzel/exopa-lab.git, with a bit of clean-up and generalizing it might be worth adding to the MESA community marketplace/add-ons.

[3] This old pipeline is my original work from the Stellar Structure and Evolution course in 2021. See https://gitlab.com/lukas_welzel/sse-mesa-lab.
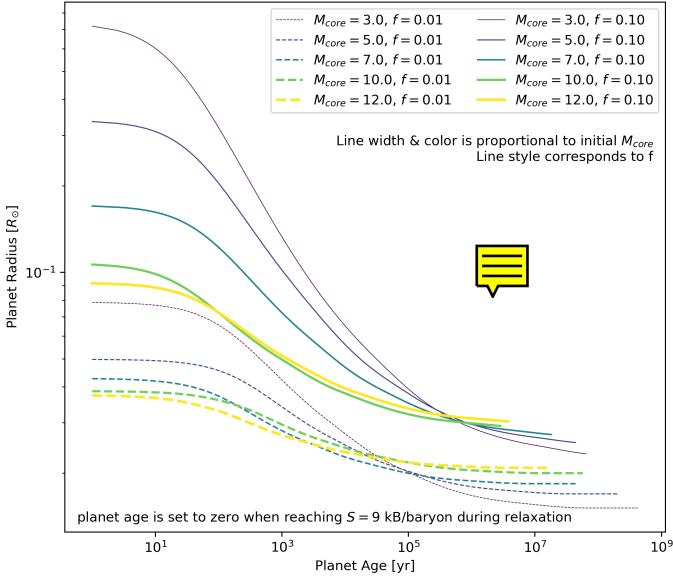
Fig. 1. The planets contract over time, counteracting their loss of energy via the Kelvin–Helmholtz mechanism. After some Myr the radius starts to decrease asymptotically as the artificial internal luminosity and partial degeneracy counteracts further contraction and the planet starts to *slowly* approach a stable equilibrium. Planets with larger core masses are initially more compact, however their final radius is larger than for lower core masses, see also Figure 3. Planets with higher envelope mass fractions are inflated due to the lower density of the gas in the envelope. In this figure the planet age is set to zero when the mean entropy reaches $S = 9\mathrm{kB}/baryon$ during relaxation of the planet. This point is reached later for planets with larger core masses as the artificial inflation mechanism we use is less efficient for more massive cores.

more efficient for these envelopes, see Figure 2, leading to a larger part of the interior being able to radiate heat because of a larger mean free path. Planets with larger core masses are initially more compact; however, their final radius is greater than that of planets with smaller core masses, as they are also more massive in general. This no longer holds for massive gas giants where an increase in mass and thus gravitational potential leads to a decrease in scale height due to further compression of the gas envelope and phase change in the interior. (Bashi et al. 2017) The results of the simulations generally overlap with observed age/mass-radius relationship, however since the planets are somewhat near the transition between two regimes for the mass-radius relationships (Bashi et al. 2017), are old and not externally heated (Sarkis et al. 2021) and also Wu et al. (2012) regarding re-inflation of Jupiters) the planets contract too much compared to observed exoplanets, even in extreme cases (Linder et al. 2019; Kubyshkina et al. 2022).

$$L = \frac{dU}{dt} \propto \frac{d}{dt}\frac{M^2}{R} \approx \frac{M^2}{R^2}\frac{dR}{dt}, \qquad (3)$$

from the Virial theorem, where we make simplifying assumptions about constant composition, EOS & ratio of heats, no internal energy production or mass loss, the latter of which are somewhat valid for slowly contracting planets without strong stellar irradiation.

3.2. Final Mass and Radius

The final radius and mass relation of the planets is shown in Figure 3. The sample of simulated planets shows a strong power-law

relationship between final radius and planet mass. These relation has been extensively explored in the literature since it is relevant for inferring the planet mass or radius from its counterpart when only one can be observed (e.g. radial velocity vs. transits respectively). Nevertheless, there are alternative non-parametric approaches which avoid some of the problematic power-law assumptions, e.g. Ning et al. (2018). In this work we focus on power laws due to their simplicity. In the literature these relations are typically constructed from a population of (comparable) exoplanets, however, since we simulate the planets in unnaturally similar conditions that do not cover the total set of exoplanets we find a slightly different mass-radius relation. We fit the exponent of Equation 4 to both f populations simultaneously, while letting the offset parameter $k(f)$ vary independently. We find that a scaling parameter a does not significantly improve the fit and hence we set it to unity.

$$R_P(M_P)_{t\to\infty} = aM_P^{0.29\pm0.005} + k(f), \text{ with } a = 1, \qquad (4)$$

where $k(f)$ is an offset to fit different envelope mass fractions and a a proportionality factor.

Comparing our result to the work of Weiss et al. (2013); Chen et al. (2016b); Bashi et al. (2017) we find a lower exponent due to the peculiarities sample of planets in ExoP-Lab as highlighted in section 3.1. More recent work (Ulmer-Moll et al. 2019) focuses on more complex estimators which can reproduce the high variance, especially for large mass planets, which we naturally do not observe in the ExoP-Lab sample. We note only that the current setup of our experiments is unable to cover the whole space of exoplanets, e.g. equilibrium temperature (Guillot 2005), stellar metallicity (Buchhave et al. 2014; Narang et al. 2018), composition Lopez et al. (2014), or irradiation (Enoch et al. 2012) and are thus unable to reproduce the diversity in planet radii. Instead we recover the power law expected for the increase against further compression as the planet mass is increased while staying under the critical transition mass. Lastly, we note that we expect the M-R relation for these low mass/low compression planets to be relatively sensitive to composition, however the simulated planets are dominated by a H-He mixture and are thus following a power-law that is unexpectedly close to that of observed gas giants with $M\ 120\ M_\oplus$ where the H-He equation of state (EOS) dominated the M-R relationship, see section 3.4. (Bashi et al. 2017)

3.3. Stability

The radiative and convective gradients of the planets are plotted against their fractional radius in Figure 2. There are two criteria for stability against convection in gas planets, the Schwarzschild criterion (SC) and Ledoux criterion (LC), in Equation 5 and Equation 6 respectively.

$$\mathcal{Y}_S \equiv \nabla_{\rm rad} - \nabla_{\rm ad} < 0 \qquad (5)$$

$$\mathcal{Y}_L \equiv \nabla_{\rm rad} + \frac{\chi_\mu}{\chi_T}\nabla_\mu - \nabla_{\rm ad} < 0, \qquad (6)$$

where $\nabla \equiv d\ln P/d\ln T$ is the temperature gradient (see Figure 5) for adiabatic or radiative heat transport and $\nabla_\mu = d\ln\mu/d\ln P$ the composition gradient with χ_μ, χ_T the gradients at constant density and temperature T or mean mol. weight μ, respectively.

In the following we will use the SC for determining stability, due to two reasons; a) for old, slowly changing planets without ongoing, however with past entrainment the SC and LC are
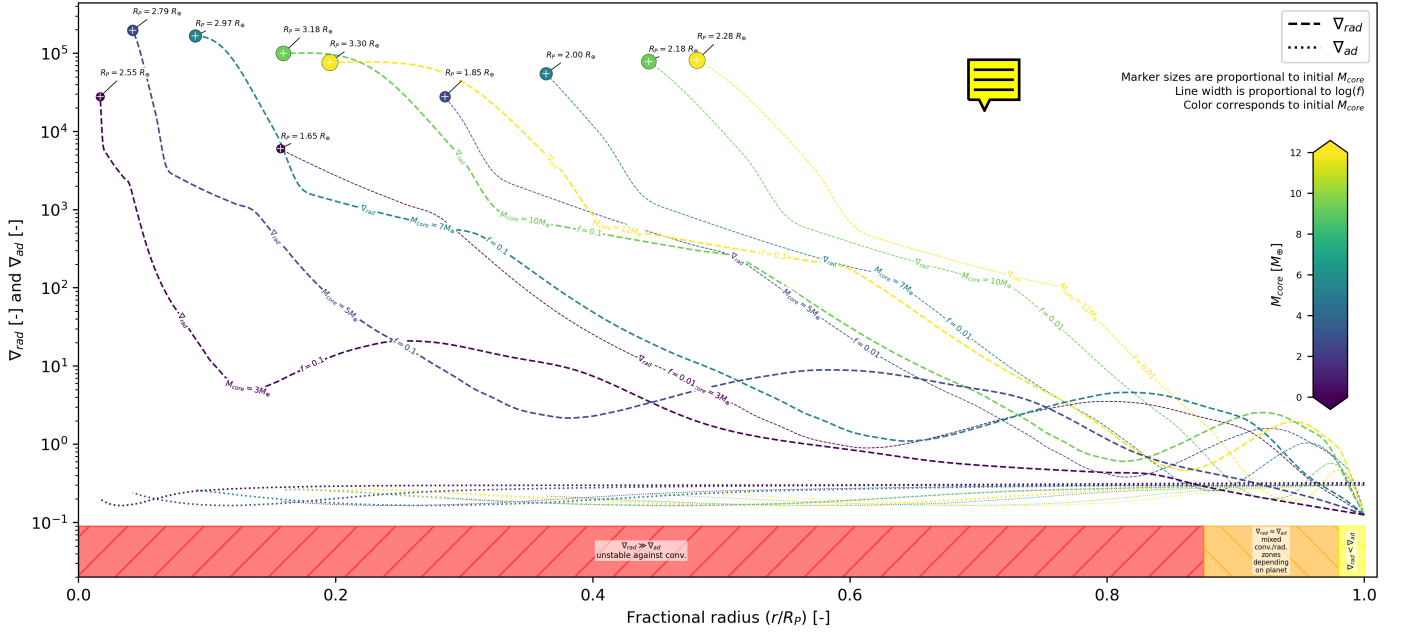
Fig. 2. The final planet interior is strongly convective for the majority of its radius, up to $\sim 0.8 r/R_P$. At larger radii the interior has regions where the radiative gradient is low enough to stabilize the interior against convection. The very outer atmosphere of the planet ($0.95 \lesssim r/R_P$) is stable as the opacity of the medium decreases and radiative heat transfer becomes efficient. Note that we only evaluate the Schwarzschild criterion (SC) for stability instead of the Ledoux criterion (LC) since the evolutionary time-scale at at the final simulated ages is much larger than the convective time-scale and hence the SC is equivalent to the LC (Anders et al. 2022b). Planets with large envelope fractions and/or (core) masses are less stable against convection for larger parts of their interior. For heavy planets with large envelope fractions the outer 20% of the planet can have an isolated non-convective layer of fractional size $\sim 2\%$, however more complex phenomena might disrupt this zone, see section 3.3.1.

equivalent due to the mixing of the interior over $\gtrsim$ 100 convective overturn timescales (Anders et al. 2022b), and b) our simulated planets are dominated by H-He so that the composition gradient is less relevant, when neglecting poorly understood regions of the EOS such stratification due to He rainout (Mankovich et al. 2020), which might not be part of the interior profile in any case (Nettelmann et al. 2015), see also section 3.4.

We find that the interior of the simulated planets is highly convective up to radius fraction of $\sim 95\%$ after which low core mass planets become fully radiative. Nevertheless, large core mass and low envelope mass fraction planets have a radiative zone, again a convective zone and only then become fully radiative for the last $\sim 1\%$ of radius, when considering just the SC.

3.3.1. Stability of Isolated Radiative Layers

As highlighted above, large core mass and envelope mass fraction planets seem to have a more complicated structure in the outer 20% of their radius. However, convection is a dynamic process which is prone to overshoot due to the bulk fluid momentum, see Figure 4.[4] This process happens at the convective-radiative boundary as well as the inverse so that the thickness of radiative layers can be depressed compared to convective layers. This means that the isolated radiative zones in Figure 2 might be smaller than shown or fully convective. MESA incorporates an approximation of this convective boundary mixing (Paxton et al. 2013), however this feature is not enabled in the simulations. (Anders et al. 2022c,a; Leconte et al. 2012)

3.4. Phase Profile

The final temperature-pressure (TP) profiles of the planets together with hydrogen (H) and helium (He) phase diagrams are shown in Figure 5. The profiles are close to a polytrope with a polytropic index of $n = 1.3$ so that $1 < n < \gamma(xH + yHe)$ for a H-He mixture is a good assumption for the supermajority of the interior. The largest deviations from this polytrope occur near the phase transition of H and H-He mixtures. This is because the EOS deviate strongly from polytropes near these phase transitions. The tracks of planets with high core mass and low envelope fraction deviate from the closely matched tracks of the other planets hear the region where H and He smoothly dissociate, which indicates that there might be rainout of He at parts in the interior which creates a significantly different structure and TP profile to the other planets. The very deep interior of the heaviest simulated planets might contain liquid metallic hydrogen, which could lead to induced magnetic fields originating from their cores (Zaghoo et al. 2017, 2018). Comparing the simulated profiles to the profiles of Jupiter and Saturn shows the impact of a more complex composition and high heavy element mass fraction and higher masses (Mankovich et al. 2021; Nettelmann et al. 2021). The atmosphere of the heavier gas giants is much hotter, whereas the deep interior is cooled relative to the simulated planets. This might be a sign of more efficient heat transport in the potentially dilute cores of Jupiter and Saturn together with an insulating He-rain layer and/or an effect of the artificial internal luminosity of the simulated planets. (Liu et al. 2019; Helled et al. 2022; Miguel et al. 2023a)

---

[4] I also found this Garai et al. (2022) which puts the phenomena into a bit more familiar scales.
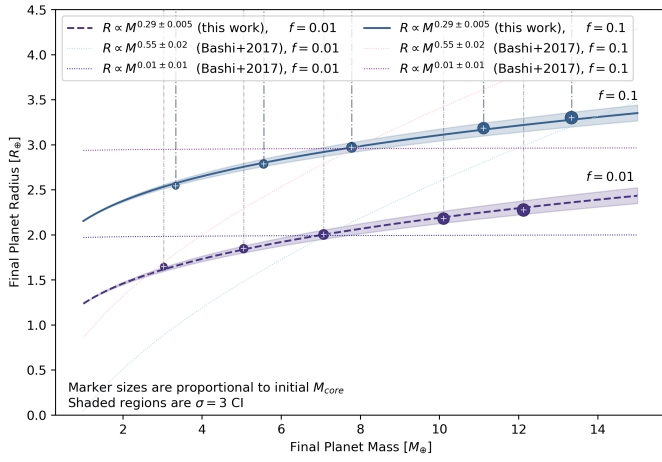
Fig. 3. The final planet radius of the planets in ExoP-Lab implies a power-law relation with the final planet mass that holds for both envelope mass fractions, when accounting for the difference in f with an offset, see Equation 4. The power-law that we find in this work agrees with the power-laws that would be expected for old, medium-sized gas planets based on those reported in the literature (e.g. Weiss et al. (2013); Chen et al. (2016b); Bashi et al. (2017)). The curves of Bashi et al. (2017) correspond to two regimes (small planets $R \propto M^{0.55\pm0.02}$ and large planets $R \propto M^{0.01\pm0.01}$) found in their data, with the transition at $12.1 \pm 0.5 R_\oplus$. Note that while Weiss et al. (2013); Chen et al. (2016b); Bashi et al. (2017) construct their relations based on a set of observed planets at different ages, the planets in this figure are 10^{7-9} yrs old and are only internally heated. Since our experiment does not simulate mass loss the planet mass does not change over time as can be seen in the vertical lines which are the radius-planet mass tracks over the planet evolution.
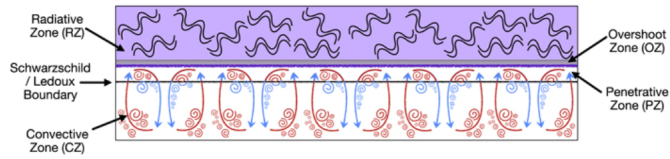
Fig. 4. Schematic of convective overshoot and penetrative zone at the convective-radiative boundary. The process is equivalent at radiative-convective boundary so that the thickness of radiative zones is depressed compared to convective zones. (Anders et al. 2022c)

3.4.1. Polytrope & H-He Dissociation

We fit a simple polytrope (linear fit in log-log) to the simulated PT profiles. Recently there has been interest in extending the simple polytrope profiles to composite curves which can better follow tracks over phase transitions. (Kadam 2021) Such a model would be very suitable to the analysis in this work since the PT tracks in Figure 5 undergo only one clear phase transition and a bipolytrope could better indicate if the deviation of the large core mass, low envelope mass fraction planets do pass through a H-He dissociation region (analogous to the effect described by Vorberger et al. (2007)) or if a different mechanism is responsible for their departure. (Baumeister et al. 2018; Paul et al. 2014)

4. Discussion

This work relies on the simulation of gas planets using MESA, however fully understanding the MESA software package and what happens under the hood as well as how this influences the results requires much more time than was possible to spend on
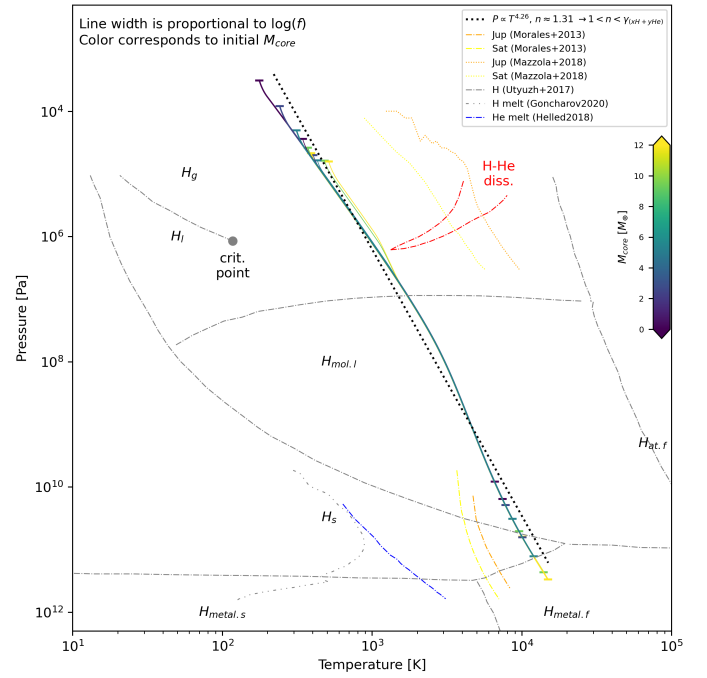
Fig. 5. The temperature-pressure (TP) profile of the planets at 10^{7-9} yrs are close to a power law with exponent 4.25 or a polytropic index of ~ 1.3. Furthermore, the profiles for all planets are very similar at high pressures, roughly after the transition of hydrogen from a liquid to a molecular liquid. The deviation from the polytrope increase near phase transitions of hydrogen (and H-He mixtures), see section 3.4.1. The tracks for heavy planets with small envelope mass fractions separates significantly from the other tracks near the hydrogen-helium disassociation zone (Vorberger et al. 2007), see section 3.4.1. The latter two points are especially clear when comparing the simulated planets with the profiles of Jupiter and Saturn (Mazzola et al. (2018,?) for low and high pressure respectively) where these effects are exaggerated due to their higher internal pressure as well as head deposition into their envelope (Kadam 2021).

this project. Furthermore, the provided simulation setup does not by itself cover the conditions the planet is placed in w.r.t. stellar environment and physics solved by MESA. This severely limits the applicability of the results presented in this study. Nevertheless, we draw conclusions by comparing our results to previous work, both simulated and observed, and find general agreement. Where there is no agreement, it is difficult to say with certainty if this is due to the simulation settings or some other option. In above work we favour explanations that highlight physical over numerical modeling differences.

In part of this analysis we rely on the large body of work on Jupiter(s) and Saturn due to the relative lack of work and certainty on Neptune, Uranus and more importantly sub-Neptunes which more closely resemble the simulated planets. This means that we expect blind spots or bias when it comes to the impact of composition and EOS together with the potential for comparing the simulated sample to population studies with dissimilar planets in radically different regimes. We highlight these differences were we think they might have an impact.

5. Conclusion

We analyse a simulated sample of sub-Neptune exoplanet with varying initial core mass and envelope mass fraction. We find that the simulated planets evolve asymptotically towards a lower equilibrium radius as they age due to contraction as they radi-

ate energy. We find rough agreement with the broader body of work for their mass-radius relation, and propose that the differences are explained by the dissimilar population samples and (lack of) stellar environment. We further find that the planets are mostly convective with only the upper 2% being radiative. We highlight that radiative zones in between convective zones might be disrupted by convective boundary mixing. Lastly, we find that the interior of the planets closely follow a polytrope and deviate near phase transitions. We highlight the potential for induced magnetic fields for sub-Neptunes with fluid metallic hydrogen. Lastly we give a critical reflection of the work and uncertainties due to MESA and the relative lack of sub-Neptune surveys.

References

Anders, E. H., Jermyn, A. S., Lecoanet, D., & Brown, B. P. 2022a, The Astrophysical Journal, 926, 169

Anders, E. H., Jermyn, A. S., Lecoanet, D., et al. 2022b, The Astrophysical Journal Letters, 928, L10

Anders, E. H., Jermyn, A. S., Lecoanet, D., et al. 2022c, Research Notes of the AAS, 6, 41

Angulo, C., Arnould, M., Rayet, M., et al. 1999, Nucl. Phys. A, 656, 3

Bashi, D., Helled, R., Zucker, S., & Mordasini, C. 2017, Astronomy & Astrophysics, 604, A83

Baumeister, P., MacKenzie, J., Tosi, N., & Godolt, M. 2018, in European Planetary Science Congress, EPSC2018–678

Blouin, S., Shaffer, N. R., Saumon, D., & Starrett, C. E. 2020, ApJ, 899, 46

Buchhave, L. A., Bizzarro, M., Latham, D. W., et al. 2014, Nature, 509, 593

Cassisi, S., Potekhin, A. Y., Pietrinferni, A., Catelan, M., & Salaris, M. 2007, ApJ, 661, 1094

Chen, H. & Rogers, L. A. 2016a, The Astrophysical Journal, 831, 180

Chen, J. & Kipping, D. 2016b, The Astrophysical Journal, 834, 17

Chugunov, A. I., Dewitt, H. E., & Yakovlev, D. G. 2007, Phys. Rev. D, 76, 025028

Cyburt, R. H., Amthor, A. M., Ferguson, R., et al. 2010, ApJS, 189, 240

Enoch, B., Cameron, A. C., & Horne, K. 2012, Astronomy & Astrophysics, 540, A99

Ferguson, J. W., Alexander, D. R., Allard, F., et al. 2005, ApJ, 623, 585

Fuller, G. M., Fowler, W. A., & Newman, M. J. 1985, ApJ, 293, 1

Garai, S. & Sahoo, S. 2022, Physics of Fluids, 34, 124101

Guillot, T. 2005, Annu. Rev. Earth Planet. Sci., 33, 493

Helled, R., Stevenson, D. J., Lunine, J. I., et al. 2022, Icarus, 114937

Iglesias, C. A. & Rogers, F. J. 1993, ApJ, 412, 752

Iglesias, C. A. & Rogers, F. J. 1996, ApJ, 464, 943

Irwin, A. W. 2004, The FreeEOS Code for Calculating the Equation of State for Stellar Interiors

Itoh, N., Hayashi, H., Nishikawa, A., & Kohyama, Y. 1996, ApJS, 102, 411

Jermyn, A. S., Bauer, E. B., Schwab, J., et al. 2023, ApJS, 265, 15

Jermyn, A. S., Schwab, J., Bauer, E., Timmes, F. X., & Potekhin, A. Y. 2021, ApJ, 913, 72

Kadam, K. 2021, Research Notes of the AAS, 5, 202

Kubyshkina, D. & Fossati, L. 2022, Astronomy & Astrophysics, 668, A178

Langanke, K. & Martínez-Pinedo, G. 2000, Nuclear Physics A, 673, 481

Leconte, J. & Chabrier, G. 2012, Astronomy & Astrophysics, 540, A20

Linder, E. F., Mordasini, C., Mollière, P., et al. 2019, Astronomy & Astrophysics, 623, A85

Liu, S.-F., Hori, Y., Müller, S., et al. 2019, Nature, 572, 355

Lopez, E. D. & Fortney, J. J. 2014, The Astrophysical Journal, 792, 1

Malsky, I. & Rogers, L. A. 2020, The Astrophysical Journal, 896, 48

Mankovich, C. R. & Fortney, J. J. 2020, The Astrophysical Journal, 889, 51

Mankovich, C. R. & Fuller, J. 2021, Nature Astronomy, 5, 1103

Mazzola, G., Helled, R., & Sorella, S. 2018, Physical Review Letters, 120, 025701

Miguel, Y. & Vazan, A. 2023a, Remote Sensing, 15, 681

Miguel, Y., Zhang, Y., & van Buchem, C. 2023b, Exo-planets A: Interiors and Atmospheres - 2023 Lab Assignment

Narang, M., Manoj, P., Furlan, E., et al. 2018, The astronomical journal, 156, 221

Nettelmann, N., Fortney, J., Moore, K., & Mankovich, C. 2015, Monthly Notices of the Royal Astronomical Society, 447, 3422

Nettelmann, N., Movshovitz, N., Ni, D., et al. 2021, The Planetary Science Journal, 2, 241

Ning, B., Wolfgang, A., & Ghosh, S. 2018, The Astrophysical Journal, 869, 5

Oda, T., Hino, M., Muto, K., Takahara, M., & Sato, K. 1994, Atomic Data and Nuclear Data Tables, 56, 231

Paul, G. C., Barman, M. C., & Mohit, A. A. 2014, NRIAG Journal of Astronomy and Geophysics, 3, 163

Paxton, B., Bildsten, L., Dotter, A., et al. 2011, ApJS, 192, 3

Paxton, B., Cantiello, M., Arras, P., et al. 2013, ApJS, 208, 4

Paxton, B., Marchant, P., Schwab, J., et al. 2015, ApJS, 220, 15

Paxton, B., Schwab, J., Bauer, E. B., et al. 2018, ApJS, 234, 34

Paxton, B., Smolec, R., Schwab, J., et al. 2019, ApJS, 243, 10

Potekhin, A. Y. & Chabrier, G. 2010, Contributions to Plasma Physics, 50, 82

Poutanen, J. 2017, ApJ, 835, 119

Rogers, F. J. & Nayfonov, A. 2002, ApJ, 576, 1064

Sarkis, P., Mordasini, C., Henning, T., Marleau, G. D., & Mollière, P. 2021, Astronomy & Astrophysics, 645, A79

Saumon, D., Chabrier, G., & van Horn, H. M. 1995, ApJS, 99, 713

Timmes, F. X. & Swesty, F. D. 2000, ApJS, 126, 501

Ulmer-Moll, S., Santos, N., Figueira, P., Brinchmann, J., & Faria, J. 2019, Astronomy & Astrophysics, 630, A135

Vorberger, J., Tamblyn, I., Militzer, B., & Bonev, S. 2007, Physical Review B, 75, 024206

Weiss, L. M., Marcy, G. W., Rowe, J. F., et al. 2013, The Astrophysical Journal, 768, 14

Welzel, L. & Lin, L. 2021, Stellar Structure and Evolution course 2021 - Modules for Experiments in Stellar Astrophysics (MESA1) Laboratory. Lecturer Serena Viti, Leiden University., code repository https://gitlab.com/lukas_welzel/sse-mesa-lab.

Wu, Y. & Lithwick, Y. 2012, The Astrophysical Journal, 763, 13

Zaghoo, M. & Collins, G. 2018, The Astrophysical Journal, 862, 19

Zaghoo, M. & Silvera, I. F. 2017, Proceedings of the National Academy of Sciences, 114, 11873

Appendix A: Appendix

Appendix A.1: Notes on content in Appendix

The content in the appendix is either to show the required plots so that you can more easily compare them with the ones that you have probably produced (section A.3.2), extra data that does not need to be in the main body of the essay such as the experiment setup (section A.3.3) or software citations (section A.2).

Appendix A.2: MESA

The MESA EOS is a blend of the OPAL (Rogers et al. 2002), SCVH (Saumon et al. 1995), FreeEOS (Irwin 2004), HELM (Timmes et al. 2000), PC (Potekhin et al. 2010), and Skye (Jermyn et al. 2021) EOSes.

Radiative opacities are primarily from OPAL (Iglesias et al. 1993, 1996), with low-temperature data from Ferguson et al. (2005) and the high-temperature, Compton-scattering dominated regime by Poutanen (2017). Electron conduction opacities are from Cassisi et al. (2007) and Blouin et al. (2020).

Nuclear reaction rates are from JINA REACLIB (Cyburt et al. 2010), NACRE (Angulo et al. 1999) and additional tabulated weak reaction rates Fuller et al. (1985); Oda et al. (1994); Langanke et al. (2000). Screening is included via the prescription of Chugunov et al. (2007). Thermal neutrino loss rates are from Itoh et al. (1996).

Appendix A.3: Experiments

Appendix A.3.1: Failed Experiments

Experiments fail because we manually set the initial mass and radius. If MESA finds values exceeding these bounds during the evolution the experiment is terminated. All configurations are shown in Figure A.1.
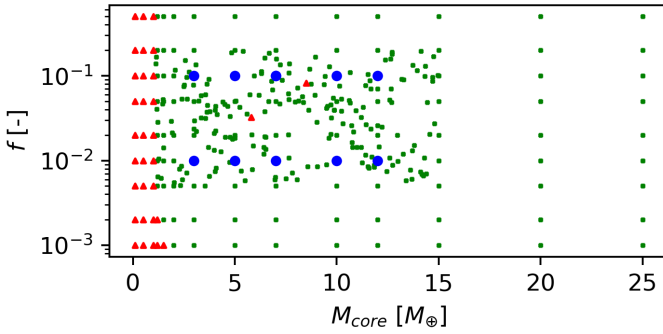
Fig. A.1. Overview of the experiments, including only planets that have been simulated for 5 Gyr. The RS covers a regions slightly larger than the required experiments whereas the GS covers a wide range of core masses and envelope fractions. Planets with very small core masses cannot be simulated by MESA and it would in any case have very different compositions than we assume here (Chen et al. 2016a; Malsky et al. 2020). The two failed experiments in the RS region failed for a different reason without throwing an exception recognized by `mesa_runner.py`.

Appendix A.3.2: Additional Plots

(No time)

Appendix A.3.3: Experiment Setup

(next page)

Table A.1. Experiment data.

ID	M_{core} [$M_\oplus$]	f [-]	Age ($t = 0$) [yr]	Age ($t = t_{final}$) [yr]	$R_P(t = 0)$ [$R_\oplus$]	$R_P(t = t_{final}$) [$R_\oplus$]	M_P [$M_\oplus$]
0	1.00×10^1	1.00×10^{-3}	2.54×10^1	5.00×10^9	2.78×10^0	1.95×10^0	1.00×10^1
1	1.00×10^1	2.00×10^{-3}	1.68×10^1	5.00×10^9	3.06×10^0	1.99×10^0	1.00×10^1
2	1.00×10^1	5.00×10^{-3}	4.56×10^1	5.00×10^9	3.59×10^0	2.08×10^0	1.01×10^1
3	1.00×10^1	1.00×10^{-2}	8.75×10^1	5.00×10^9	4.21×10^0	2.18×10^0	1.01×10^1
4	1.00×10^1	2.00×10^{-2}	4.09×10^2	5.00×10^9	5.17×10^0	2.34×10^0	1.02×10^1
5	1.00×10^1	5.00×10^{-2}	1.01×10^3	5.00×10^9	7.71×10^0	2.70×10^0	1.05×10^1
6	1.00×10^1	1.00×10^{-1}	1.77×10^3	5.00×10^9	1.16×10^1	3.18×10^0	1.11×10^1
7	1.00×10^1	2.00×10^{-1}	3.60×10^3	5.00×10^9	1.92×10^1	3.98×10^0	1.25×10^1
8	1.00×10^1	5.00×10^{-1}	1.55×10^7	5.00×10^9	1.05×10^1	6.01×10^0	2.00×10^1
9	1.01×10^1	7.62×10^{-2}	6.58×10^2	5.00×10^9	9.70×10^0	2.97×10^0	1.10×10^1
10	1.02×10^1	5.31×10^{-2}	5.11×10^2	5.00×10^9	7.89×10^0	2.75×10^0	1.08×10^1
11	1.02×10^1	3.83×10^{-2}	8.88×10^2	5.00×10^9	6.68×10^0	2.59×10^0	1.06×10^1
12	1.03×10^1	2.71×10^{-2}	6.27×10^2	5.00×10^9	5.73×10^0	2.45×10^0	1.06×10^1
13	1.06×10^1	5.15×10^{-2}	1.22×10^3	5.00×10^9	7.53×10^0	2.75×10^0	1.12×10^1
14	1.07×10^1	4.82×10^{-2}	5.30×10^2	5.00×10^9	7.27×10^0	2.72×10^0	1.12×10^1
15	1.07×10^1	1.09×10^{-1}	1.04×10^3	5.00×10^9	1.16×10^1	3.30×10^0	1.20×10^1
16	1.07×10^1	2.60×10^{-2}	2.82×10^2	5.00×10^9	5.59×10^0	2.46×10^0	1.10×10^1
17	1.08×10^1	1.63×10^{-2}	3.56×10^2	5.00×10^9	4.74×10^0	2.32×10^0	1.09×10^1
18	1.08×10^1	1.44×10^{-2}	1.43×10^2	5.00×10^9	4.57×10^0	2.30×10^0	1.09×10^1
19	1.08×10^1	2.18×10^{-2}	4.94×10^2	5.00×10^9	5.21×10^0	2.41×10^0	1.11×10^1
20	1.09×10^1	3.88×10^{-2}	4.73×10^2	5.00×10^9	6.53×10^0	2.63×10^0	1.14×10^1
21	1.10×10^1	1.44×10^{-2}	3.22×10^2	5.00×10^9	4.54×10^0	2.30×10^0	1.11×10^1
22	1.12×10^1	3.22×10^{-2}	3.92×10^2	5.00×10^9	5.96×10^0	2.56×10^0	1.16×10^1
23	1.12×10^1	1.44×10^{-2}	1.53×10^2	5.00×10^9	4.54×10^0	2.32×10^0	1.14×10^1
24	1.12×10^1	9.42×10^{-3}	1.06×10^2	5.00×10^9	4.06×10^0	2.23×10^0	1.14×10^1
25	1.13×10^1	4.28×10^{-2}	5.54×10^2	5.00×10^9	6.71×10^0	2.69×10^0	1.18×10^1
26	1.14×10^1	7.66×10^{-2}	2.01×10^3	5.00×10^9	8.89×10^0	3.05×10^0	1.23×10^1
27	1.14×10^1	1.17×10^{-2}	2.95×10^2	5.00×10^9	4.27×10^0	2.28×10^0	1.15×10^1
28	1.14×10^1	2.65×10^{-2}	6.78×10^2	5.00×10^9	5.47×10^0	2.50×10^0	1.17×10^1
29	1.15×10^1	1.04×10^{-1}	1.24×10^3	5.00×10^9	1.06×10^1	3.31×10^0	1.29×10^1
30	1.15×10^1	8.52×10^{-3}	1.02×10^2	5.00×10^9	3.95×10^0	2.23×10^0	1.16×10^1
31	1.16×10^1	8.14×10^{-3}	2.10×10^2	5.00×10^9	3.88×10^0	2.22×10^0	1.17×10^1
32	1.16×10^1	8.79×10^{-2}	2.38×10^3	5.00×10^9	9.46×10^0	3.17×10^0	1.28×10^1
33	1.17×10^1	2.36×10^{-2}	2.76×10^2	5.00×10^9	5.24×10^0	2.48×10^0	1.19×10^1
34	1.17×10^1	7.00×10^{-2}	9.03×10^2	5.00×10^9	8.36×10^0	3.00×10^0	1.26×10^1
35	1.17×10^1	1.10×10^{-2}	2.96×10^2	5.00×10^9	4.19×10^0	2.28×10^0	1.18×10^1
36	1.18×10^1	8.39×10^{-3}	2.28×10^2	5.00×10^9	3.90×10^0	2.24×10^0	1.19×10^1
37	1.18×10^1	8.87×10^{-3}	1.11×10^2	5.00×10^9	3.97×10^0	2.25×10^0	1.20×10^1
38	1.20×10^1	2.61×10^{-2}	3.25×10^2	5.00×10^9	5.39×10^0	2.53×10^0	1.23×10^1
39	1.20×10^1	1.00×10^{-3}	4.47×10^1	5.00×10^9	2.78×10^0	2.04×10^0	1.20×10^1
40	1.20×10^1	2.00×10^{-3}	4.71×10^1	5.00×10^9	3.04×10^0	2.08×10^0	1.20×10^1
41	1.20×10^1	5.00×10^{-3}	1.36×10^2	5.00×10^9	3.51×10^0	2.17×10^0	1.21×10^1
42	1.20×10^1	1.00×10^{-2}	2.80×10^2	5.00×10^9	4.06×10^0	2.28×10^0	1.21×10^1
43	1.20×10^1	2.00×10^{-2}	2.44×10^2	5.00×10^9	4.93×10^0	2.44×10^0	1.22×10^1
44	1.20×10^1	5.00×10^{-2}	1.60×10^3	5.00×10^9	6.96×10^0	2.81×10^0	1.26×10^1
45	1.20×10^1	1.00×10^{-1}	1.32×10^3	5.00×10^9	1.00×10^1	3.30×10^0	1.33×10^1
46	1.20×10^1	2.00×10^{-1}	5.81×10^3	5.00×10^9	1.54×10^1	4.11×10^0	1.50×10^1
47	1.20×10^1	5.00×10^{-1}	1.91×10^7	5.00×10^9	1.01×10^1	6.17×10^0	2.40×10^1
48	1.20×10^1	7.05×10^{-2}	9.70×10^2	5.00×10^9	8.28×10^0	3.02×10^0	1.29×10^1
49	1.21×10^1	1.45×10^{-2}	1.83×10^2	5.00×10^9	4.47×10^0	2.36×10^0	1.22×10^1
50	1.22×10^1	2.48×10^{-2}	3.16×10^2	5.00×10^9	5.26×10^0	2.52×10^0	1.25×10^1
51	1.24×10^1	1.55×10^{-1}	5.07×10^3	5.00×10^9	1.27×10^1	3.79×10^0	1.46×10^1
52	1.25×10^1	7.41×10^{-3}	2.17×10^2	5.00×10^9	3.77×10^0	2.24×10^0	1.26×10^1
53	1.26×10^1	1.07×10^{-2}	1.50×10^2	5.00×10^9	4.12×10^0	2.32×10^0	1.27×10^1

ID	M_{core} [$M_\oplus$]	f [-]	Age ($t = 0$) [yr]	Age ($t = t_{final}$) [yr]	$R_P(t = 0)$ [$R_\oplus$]	$R_P(t = t_{final})$ [$R_\oplus$]	M_P [$M_\oplus$]
54	1.26×10^1	5.19×10^{-2}	8.41×10^2	5.00×10^9	6.97×10^0	2.86×10^0	1.33×10^1
55	1.26×10^1	1.58×10^{-1}	5.53×10^3	5.00×10^9	1.26×10^1	3.82×10^0	1.50×10^1
56	1.27×10^1	7.01×10^{-2}	1.11×10^3	5.00×10^9	8.01×10^0	3.05×10^0	1.36×10^1
57	1.27×10^1	4.87×10^{-2}	1.76×10^3	5.00×10^9	6.73×10^0	2.83×10^0	1.33×10^1
58	1.27×10^1	1.81×10^{-1}	3.14×10^3	5.00×10^9	1.39×10^1	4.01×10^0	1.55×10^1
59	1.27×10^1	1.91×10^{-1}	3.42×10^3	5.00×10^9	1.42×10^1	4.09×10^0	1.57×10^1
60	1.27×10^1	8.83×10^{-3}	1.26×10^2	5.00×10^9	3.94×10^0	2.29×10^0	1.28×10^1
61	1.30×10^1	2.01×10^{-2}	2.88×10^2	5.00×10^9	4.85×10^0	2.49×10^0	1.32×10^1
62	1.30×10^1	9.80×10^{-3}	1.47×10^2	5.00×10^9	4.01×10^0	2.32×10^0	1.31×10^1
63	1.32×10^1	9.16×10^{-2}	3.42×10^3	5.00×10^9	8.98×10^0	3.29×10^0	1.45×10^1
64	1.33×10^1	1.19×10^{-2}	1.82×10^2	5.00×10^9	4.19×10^0	2.37×10^0	1.34×10^1
65	1.33×10^1	9.00×10^{-2}	3.45×10^3	5.00×10^9	8.79×10^0	3.28×10^0	1.46×10^1
66	1.34×10^1	5.82×10^{-3}	1.92×10^2	5.00×10^9	3.59×10^0	2.25×10^0	1.35×10^1
67	1.36×10^1	7.70×10^{-3}	2.64×10^2	5.00×10^9	3.78×10^0	2.30×10^0	1.37×10^1
68	1.37×10^1	6.06×10^{-3}	9.52×10^1	5.00×10^9	3.61×10^0	2.27×10^0	1.38×10^1
69	1.37×10^1	1.31×10^{-2}	2.17×10^2	5.00×10^9	4.28×10^0	2.41×10^0	1.39×10^1
70	1.37×10^1	1.33×10^{-1}	2.57×10^3	5.00×10^9	1.08×10^1	3.68×10^0	1.58×10^1
71	1.38×10^1	1.52×10^{-2}	5.50×10^2	5.00×10^9	4.42×10^0	2.45×10^0	1.40×10^1
72	1.39×10^1	1.16×10^{-1}	4.96×10^3	5.00×10^9	9.79×10^0	3.54×10^0	1.58×10^1
73	1.41×10^1	7.34×10^{-3}	1.21×10^2	5.00×10^9	3.72×10^0	2.31×10^0	1.42×10^1
74	1.41×10^1	1.94×10^{-1}	8.99×10^3	5.00×10^9	1.31×10^1	4.19×10^0	1.75×10^1
75	1.42×10^1	6.88×10^{-3}	1.15×10^2	5.00×10^9	3.68×10^0	2.30×10^0	1.43×10^1
76	1.43×10^1	6.63×10^{-3}	1.13×10^2	5.00×10^9	3.66×10^0	2.30×10^0	1.43×10^1
77	1.43×10^1	1.07×10^{-2}	1.88×10^2	5.00×10^9	4.04×10^0	2.39×10^0	1.45×10^1
78	1.43×10^1	9.91×10^{-2}	4.55×10^3	5.00×10^9	8.87×10^0	3.41×10^0	1.59×10^1
79	1.43×10^1	1.29×10^{-1}	2.75×10^3	5.00×10^9	1.03×10^1	3.68×10^0	1.65×10^1
80	1.44×10^1	6.98×10^{-3}	1.22×10^2	5.00×10^9	3.70×10^0	2.32×10^0	1.45×10^1
81	1.44×10^1	4.87×10^{-2}	1.98×10^3	5.00×10^9	6.36×10^0	2.91×10^0	1.52×10^1
82	1.46×10^1	2.05×10^{-2}	8.13×10^2	5.00×10^9	4.74×10^0	2.56×10^0	1.49×10^1
83	1.47×10^1	9.62×10^{-2}	4.71×10^3	5.00×10^9	8.66×10^0	3.40×10^0	1.63×10^1
84	1.47×10^1	8.69×10^{-2}	4.28×10^3	5.00×10^9	8.18×10^0	3.32×10^0	1.61×10^1
85	1.47×10^1	1.68×10^{-1}	4.13×10^3	4.60×10^9	1.18×10^1	4.03×10^0	1.77×10^1
86	1.48×10^1	2.74×10^{-2}	4.95×10^2	5.00×10^9	5.17×10^0	2.67×10^0	1.52×10^1
87	1.49×10^1	1.01×10^{-1}	5.18×10^3	5.00×10^9	8.81×10^0	3.46×10^0	1.66×10^1
88	1.50×10^1	1.00×10^{-3}	2.81×10^1	5.00×10^9	2.83×10^0	2.16×10^0	1.50×10^1
89	1.50×10^1	2.00×10^{-3}	6.85×10^1	5.00×10^9	3.06×10^0	2.20×10^0	1.50×10^1
90	1.50×10^1	5.00×10^{-3}	1.99×10^2	5.00×10^9	3.48×10^0	2.29×10^0	1.51×10^1
91	1.50×10^1	1.00×10^{-2}	4.26×10^2	5.00×10^9	3.96×10^0	2.40×10^0	1.52×10^1
92	1.50×10^1	2.00×10^{-2}	3.82×10^2	5.00×10^9	4.70×10^0	2.57×10^0	1.53×10^1
93	1.50×10^1	5.00×10^{-2}	2.18×10^3	5.00×10^9	6.37×10^0	2.95×10^0	1.58×10^1
94	1.50×10^1	1.00×10^{-1}	5.18×10^3	5.00×10^9	8.73×10^0	3.45×10^0	1.67×10^1
95	1.50×10^1	2.00×10^{-1}	1.08×10^4	5.00×10^9	1.28×10^1	4.28×10^0	1.87×10^1
96	1.50×10^1	5.00×10^{-1}	3.19×10^6	5.00×10^9	1.30×10^1	6.37×10^0	3.00×10^1
97	1.12×10^0	1.39×10^{-1}	7.13×10^0	5.00×10^9	1.20×10^2	2.47×10^0	1.30×10^0
98	1.15×10^0	1.68×10^{-1}	7.16×10^0	5.00×10^9	1.34×10^2	2.69×10^0	1.38×10^0
99	1.17×10^0	4.02×10^{-2}	2.04×10^0	4.10×10^3	5.96×10^1	2.25×10^1	1.22×10^0
100	1.20×10^0	5.00×10^{-3}	6.97×10^1	5.00×10^9	1.42×10^1	1.27×10^0	1.21×10^0
101	1.20×10^0	1.00×10^{-2}	4.07×10^{-1}	5.00×10^9	2.31×10^1	1.36×10^0	1.21×10^0
102	1.20×10^0	2.00×10^{-2}	1.33×10^0	5.00×10^9	3.77×10^1	1.50×10^0	1.22×10^0
103	1.20×10^0	5.00×10^{-2}	6.85×10^0	5.00×10^9	2.40×10^1	1.81×10^0	1.26×10^0
104	1.20×10^0	1.00×10^{-1}	4.99×10^0	5.00×10^9	1.01×10^2	2.21×10^0	1.33×10^0
105	1.20×10^0	2.00×10^{-1}	2.72×10^1	5.00×10^9	1.46×10^2	2.92×10^0	1.50×10^0
106	1.20×10^0	5.00×10^{-1}	2.06×10^1	5.00×10^9	2.24×10^2	4.77×10^0	2.40×10^0
107	1.21×10^0	6.47×10^{-3}	7.44×10^{-1}	5.00×10^9	1.60×10^1	1.30×10^0	1.22×10^0
108	1.22×10^0	2.84×10^{-2}	7.90×10^{-1}	5.00×10^9	4.76×10^1	1.60×10^0	1.26×10^0
							Continued on next page

ID	M_{core} [$M_\oplus$]	f [-]	Age ($t = 0$) [yr]	Age ($t = t_{final}$) [yr]	$R_P(t = 0)$ [$R_\oplus$]	$R_P(t = t_{final}$) [$R_\oplus$]	M_P [$M_\oplus$]
109	1.27×10^0	1.04×10^{-2}	9.07×10^0	5.00×10^9	6.11×10^0	1.38×10^0	1.29×10^0
110	1.37×10^0	6.19×10^{-3}	1.30×10^1	5.00×10^9	1.34×10^1	1.33×10^0	1.38×10^0
111	1.44×10^0	4.68×10^{-2}	1.83×10^0	5.00×10^9	6.36×10^1	1.84×10^0	1.51×10^0
112	1.48×10^0	5.23×10^{-2}	2.19×10^0	5.00×10^9	6.80×10^1	1.89×10^0	1.56×10^0
113	1.50×10^0	2.00×10^{-3}	6.02×10^1	5.00×10^9	7.52×10^0	1.25×10^0	1.50×10^0
114	1.50×10^0	5.00×10^{-3}	5.18×10^{-1}	5.00×10^9	1.05×10^1	1.33×10^0	1.51×10^0
115	1.50×10^0	1.00×10^{-2}	5.71×10^1	5.00×10^9	1.82×10^1	1.42×10^0	1.52×10^0
116	1.50×10^0	2.00×10^{-2}	9.81×10^{-1}	5.00×10^9	3.47×10^1	1.56×10^0	1.53×10^0
117	1.50×10^0	5.00×10^{-2}	4.40×10^0	5.00×10^9	6.58×10^1	1.88×10^0	1.58×10^0
118	1.50×10^0	1.00×10^{-1}	3.65×10^1	5.00×10^9	3.96×10^1	2.28×10^0	1.67×10^0
119	1.50×10^0	2.00×10^{-1}	1.04×10^1	5.00×10^9	1.48×10^2	2.99×10^0	1.87×10^0
120	1.50×10^0	5.00×10^{-1}	2.34×10^1	5.00×10^9	2.21×10^2	4.84×10^0	3.00×10^0
121	1.50×10^0	1.42×10^{-2}	8.30×10^{-1}	5.00×10^9	2.64×10^1	1.49×10^0	1.53×10^0
122	1.89×10^0	2.92×10^{-2}	2.27×10^0	5.00×10^9	4.06×10^1	1.74×10^0	1.95×10^0
123	1.93×10^0	2.12×10^{-2}	4.40×10^0	5.00×10^9	3.03×10^1	1.66×10^0	1.97×10^0
124	2.00×10^1	1.00×10^{-3}	1.80×10^1	5.00×10^9	2.91×10^0	2.33×10^0	2.00×10^1
125	2.00×10^1	2.00×10^{-3}	1.07×10^2	5.00×10^9	3.11×10^0	2.37×10^0	2.00×10^1
126	2.00×10^1	5.00×10^{-3}	1.48×10^2	5.00×10^9	3.49×10^0	2.46×10^0	2.01×10^1
127	2.00×10^1	1.00×10^{-2}	6.95×10^2	5.00×10^9	3.89×10^0	2.58×10^0	2.02×10^1
128	2.00×10^1	2.00×10^{-2}	1.46×10^3	5.00×10^9	4.51×10^0	2.75×10^0	2.04×10^1
129	2.00×10^1	5.00×10^{-2}	1.67×10^3	5.00×10^9	5.95×10^0	3.14×10^0	2.11×10^1
130	2.00×10^1	1.00×10^{-1}	3.80×10^3	3.17×10^9	7.85×10^0	3.68×10^0	2.22×10^1
131	2.00×10^1	2.00×10^{-1}	1.16×10^4	5.00×10^9	1.09×10^1	4.50×10^0	2.50×10^1
132	2.00×10^1	5.00×10^{-1}	2.06×10^5	5.00×10^9	1.53×10^1	6.64×10^0	4.00×10^1
133	2.50×10^1	1.00×10^{-3}	6.72×10^1	5.00×10^9	3.02×10^0	2.47×10^0	2.50×10^1
134	2.50×10^1	2.00×10^{-3}	7.58×10^1	5.00×10^9	3.20×10^0	2.52×10^0	2.50×10^1
135	2.50×10^1	5.00×10^{-3}	4.94×10^2	5.00×10^9	3.53×10^0	2.61×10^0	2.51×10^1
136	2.50×10^1	1.00×10^{-2}	1.08×10^3	5.00×10^9	3.90×10^0	2.72×10^0	2.53×10^1
137	2.50×10^1	2.00×10^{-2}	1.04×10^3	5.00×10^9	4.47×10^0	2.90×10^0	2.55×10^1
138	2.50×10^1	5.00×10^{-2}	2.73×10^3	5.00×10^9	5.73×10^0	3.30×10^0	2.63×10^1
139	2.50×10^1	1.00×10^{-1}	5.91×10^3	3.17×10^9	7.42×10^0	3.85×10^0	2.78×10^1
140	2.50×10^1	2.00×10^{-1}	3.63×10^4	5.00×10^9	9.72×10^0	4.68×10^0	3.12×10^1
141	2.50×10^1	5.00×10^{-1}	4.63×10^5	5.00×10^9	1.38×10^1	6.86×10^0	5.00×10^1
142	2.00×10^0	1.00×10^{-3}	6.66×10^0	5.00×10^9	3.13×10^0	1.30×10^0	2.00×10^0
143	2.00×10^0	2.00×10^{-3}	5.79×10^1	5.00×10^9	4.76×10^0	1.34×10^0	2.00×10^0
144	2.00×10^0	5.00×10^{-3}	4.13×10^1	5.00×10^9	7.99×10^0	1.42×10^0	2.01×10^0
145	2.00×10^0	1.00×10^{-2}	1.53×10^0	5.00×10^9	1.40×10^1	1.51×10^0	2.02×10^0
146	2.00×10^0	2.00×10^{-2}	2.13×10^0	5.00×10^9	2.75×10^1	1.65×10^0	2.04×10^0
147	2.00×10^0	5.00×10^{-2}	8.91×10^0	5.00×10^9	5.93×10^1	1.97×10^0	2.11×10^0
148	2.00×10^0	1.00×10^{-1}	2.47×10^1	5.00×10^9	3.58×10^1	2.38×10^0	2.22×10^0
149	2.00×10^0	2.00×10^{-1}	1.85×10^1	5.00×10^9	1.40×10^2	3.10×10^0	2.50×10^0
150	2.00×10^0	5.00×10^{-1}	2.00×10^3	5.00×10^9	1.70×10^2	4.95×10^0	4.00×10^0
151	2.01×10^0	5.51×10^{-3}	5.95×10^1	5.00×10^9	9.19×10^0	1.43×10^0	2.02×10^0
152	2.07×10^0	1.17×10^{-1}	1.11×10^2	5.00×10^9	1.01×10^2	2.52×10^0	2.35×10^0
153	2.27×10^0	7.97×10^{-3}	2.09×10^0	5.00×10^9	9.94×10^0	1.52×10^0	2.29×10^0
154	2.32×10^0	5.10×10^{-3}	4.09×10^0	5.00×10^9	6.88×10^0	1.47×10^0	2.33×10^0
155	2.39×10^0	8.62×10^{-3}	5.47×10^0	5.00×10^9	9.95×10^0	1.54×10^0	2.41×10^0
156	2.39×10^0	5.30×10^{-2}	1.44×10^1	5.00×10^9	5.54×10^1	2.06×10^0	2.52×10^0
157	2.43×10^0	5.97×10^{-3}	2.31×10^0	5.00×10^9	7.39×10^0	1.50×10^0	2.45×10^0
158	2.48×10^0	7.46×10^{-2}	1.58×10^1	5.00×10^9	7.17×10^1	2.26×10^0	2.68×10^0
159	2.51×10^0	7.75×10^{-2}	1.79×10^1	5.00×10^9	7.35×10^1	2.29×10^0	2.72×10^0
160	2.57×10^0	1.52×10^{-1}	3.14×10^1	5.00×10^9	1.11×10^2	2.87×10^0	3.03×10^0
161	2.63×10^0	7.19×10^{-3}	3.14×10^0	5.00×10^9	7.79×10^0	1.55×10^0	2.65×10^0
162	2.63×10^0	9.59×10^{-2}	4.92×10^1	5.00×10^9	8.36×10^1	2.46×10^0	2.91×10^0
163	2.65×10^0	5.35×10^{-2}	9.56×10^0	5.00×10^9	5.11×10^1	2.10×10^0	2.80×10^0
							Continued on next page

ID	M_{core} [$M_\oplus$]	f [-]	Age ($t = 0$) [yr]	Age ($t = t_{final}$) [yr]	$R_P(t = 0)$ [$R_\oplus$]	$R_P(t = t_{final}$) [$R_\oplus$]	M_P [$M_\oplus$]
164	2.75×10^0	1.10×10^{-1}	6.55×10^2	5.00×10^9	7.80×10^1	2.59×10^0	3.09×10^0
165	2.97×10^0	7.77×10^{-2}	4.32×10^1	5.00×10^9	6.36×10^1	2.36×10^0	3.22×10^0
166	3.00×10^0	2.35×10^{-2}	1.64×10^1	5.00×10^9	1.83×10^1	1.84×10^0	3.07×10^0
167	3.00×10^0	1.00×10^{-3}	7.76×10^1	5.00×10^9	3.53×10^0	1.43×10^0	3.00×10^0
168	3.00×10^0	2.00×10^{-3}	2.23×10^1	5.00×10^9	3.81×10^0	1.47×10^0	3.01×10^0
169	3.00×10^0	5.00×10^{-3}	6.65×10^0	5.00×10^9	5.54×10^0	1.55×10^0	3.02×10^0
170	3.00×10^0	1.00×10^{-2}	1.17×10^1	5.00×10^9	8.57×10^0	1.65×10^0	3.03×10^0
171	3.00×10^0	2.00×10^{-2}	6.88×10^0	5.00×10^9	1.56×10^1	1.80×10^0	3.06×10^0
172	3.00×10^0	5.00×10^{-2}	2.55×10^1	5.00×10^9	4.18×10^1	2.12×10^0	3.16×10^0
173	3.00×10^0	1.00×10^{-1}	7.79×10^1	5.00×10^9	7.84×10^1	2.55×10^0	3.33×10^0
174	3.00×10^0	2.00×10^{-1}	1.52×10^1	5.00×10^9	1.17×10^2	3.28×10^0	3.75×10^0
175	3.00×10^0	5.00×10^{-1}	7.11×10^2	5.00×10^9	1.71×10^2	5.15×10^0	6.00×10^0
176	3.02×10^0	2.96×10^{-2}	8.69×10^0	5.00×10^9	2.33×10^1	1.91×10^0	3.11×10^0
177	3.07×10^0	1.35×10^{-1}	2.49×10^1	5.00×10^9	9.50×10^1	2.83×10^0	3.55×10^0
178	3.12×10^0	2.20×10^{-2}	1.79×10^1	5.00×10^9	1.61×10^1	1.84×10^0	3.19×10^0
179	3.22×10^0	5.08×10^{-2}	3.17×10^1	5.00×10^9	3.82×10^1	2.15×10^0	3.39×10^0
180	3.34×10^0	5.86×10^{-2}	1.92×10^1	5.00×10^9	4.22×10^1	2.24×10^0	3.55×10^0
181	3.35×10^0	3.21×10^{-2}	1.24×10^1	5.00×10^9	2.14×10^1	1.98×10^0	3.46×10^0
182	3.54×10^0	5.05×10^{-3}	1.46×10^1	5.00×10^9	5.02×10^0	1.62×10^0	3.56×10^0
183	3.55×10^0	3.17×10^{-2}	1.47×10^1	5.00×10^9	1.89×10^1	2.00×10^0	3.67×10^0
184	3.55×10^0	6.00×10^{-2}	4.47×10^1	5.00×10^9	3.92×10^1	2.28×10^0	3.78×10^0
185	3.62×10^0	3.73×10^{-2}	3.79×10^1	5.00×10^9	2.20×10^1	2.07×10^0	3.76×10^0
186	3.64×10^0	7.99×10^{-2}	6.55×10^1	5.00×10^9	5.20×10^1	2.47×10^0	3.95×10^0
187	3.65×10^0	4.50×10^{-2}	4.33×10^1	5.00×10^9	2.64×10^1	2.15×10^0	3.82×10^0
188	3.69×10^0	1.44×10^{-2}	1.18×10^1	5.00×10^9	8.74×10^0	1.79×10^0	3.74×10^0
189	3.72×10^0	9.13×10^{-2}	4.93×10^1	5.00×10^9	5.75×10^1	2.57×10^0	4.10×10^0
190	3.75×10^0	6.57×10^{-3}	1.96×10^1	5.00×10^9	5.50×10^0	1.67×10^0	3.77×10^0
191	3.77×10^0	3.78×10^{-2}	1.94×10^1	5.00×10^9	2.08×10^1	2.09×10^0	3.91×10^0
192	3.97×10^0	1.33×10^{-2}	3.24×10^1	5.00×10^9	7.76×10^0	1.81×10^0	4.03×10^0
193	3.99×10^0	2.09×10^{-2}	3.91×10^1	5.00×10^9	1.07×10^1	1.92×10^0	4.08×10^0
194	4.04×10^0	7.43×10^{-3}	2.52×10^1	5.00×10^9	5.36×10^0	1.71×10^0	4.07×10^0
195	4.04×10^0	3.93×10^{-2}	2.43×10^1	5.00×10^9	1.88×10^1	2.13×10^0	4.21×10^0
196	4.06×10^0	2.24×10^{-2}	1.93×10^1	5.00×10^9	1.11×10^1	1.95×10^0	4.15×10^0
197	4.06×10^0	4.39×10^{-2}	5.86×10^1	5.00×10^9	2.10×10^1	2.18×10^0	4.25×10^0
198	4.08×10^0	8.15×10^{-3}	2.84×10^1	5.00×10^9	5.78×10^0	1.74×10^0	4.12×10^0
199	4.13×10^0	3.52×10^{-2}	2.48×10^1	5.00×10^9	1.64×10^1	2.10×10^0	4.28×10^0
200	4.32×10^0	1.28×10^{-2}	1.86×10^1	5.00×10^9	6.98×10^0	1.84×10^0	4.38×10^0
201	4.42×10^0	4.93×10^{-2}	8.15×10^1	5.00×10^9	2.04×10^1	2.28×10^0	4.65×10^0
202	4.49×10^0	4.62×10^{-2}	3.79×10^1	5.00×10^9	1.87×10^1	2.26×10^0	4.71×10^0
203	4.53×10^0	1.90×10^{-2}	5.67×10^1	5.00×10^9	8.52×10^0	1.95×10^0	4.62×10^0
204	4.65×10^0	4.35×10^{-2}	8.97×10^1	5.00×10^9	1.64×10^1	2.24×10^0	4.86×10^0
205	4.75×10^0	9.59×10^{-3}	2.12×10^1	5.00×10^9	5.54×10^0	1.82×10^0	4.79×10^0
206	4.77×10^0	3.32×10^{-2}	8.60×10^1	5.00×10^9	1.23×10^1	2.15×10^0	4.94×10^0
207	4.77×10^0	1.90×10^{-2}	6.65×10^1	5.00×10^9	7.97×10^0	1.97×10^0	4.87×10^0
208	4.83×10^0	1.88×10^{-1}	1.74×10^1	5.00×10^9	7.51×10^1	3.44×10^0	5.95×10^0
209	4.88×10^0	1.79×10^{-2}	3.15×10^1	5.00×10^9	7.64×10^0	1.97×10^0	4.97×10^0
210	5.00×10^0	1.00×10^{-3}	5.44×10^1	5.00×10^9	2.75×10^0	1.62×10^0	5.00×10^0
211	5.00×10^0	2.00×10^{-3}	2.54×10^1	5.00×10^9	3.25×10^0	1.66×10^0	5.01×10^0
212	5.00×10^0	5.00×10^{-3}	1.41×10^1	5.00×10^9	4.11×10^0	1.75×10^0	5.03×10^0
213	5.00×10^0	1.00×10^{-2}	2.47×10^1	5.00×10^9	5.43×10^0	1.85×10^0	5.05×10^0
214	5.00×10^0	2.00×10^{-2}	7.88×10^1	5.00×10^9	7.84×10^0	2.00×10^0	5.10×10^0
215	5.00×10^0	5.00×10^{-2}	1.23×10^2	5.00×10^9	1.65×10^1	2.34×10^0	5.26×10^0
216	5.00×10^0	1.00×10^{-1}	1.15×10^2	5.00×10^9	3.65×10^1	2.79×10^0	5.56×10^0
217	5.00×10^0	2.00×10^{-1}	1.42×10^3	5.00×10^9	6.78×10^1	3.54×10^0	6.25×10^0
218	5.00×10^0	5.00×10^{-1}	1.41×10^6	5.00×10^9	2.15×10^1	5.47×10^0	1.00×10^1
							Continued on next page

ID	M_{core} [$M_\oplus$]	f [-]	Age ($t = 0$) [yr]	Age ($t = t_{final}$) [yr]	$R_P(t = 0)$ [$R_\oplus$]	$R_P(t = t_{final}$) [$R_\oplus$]	M_P [$M_\oplus$]
219	5.01×10^0	1.83×10^{-2}	7.52×10^1	5.00×10^9	7.55×10^0	1.98×10^0	5.10×10^0
220	5.04×10^0	5.05×10^{-2}	1.26×10^2	5.00×10^9	1.65×10^1	2.35×10^0	5.31×10^0
221	5.23×10^0	4.26×10^{-2}	5.95×10^1	5.00×10^9	1.34×10^1	2.29×10^0	5.47×10^0
222	5.32×10^0	7.53×10^{-3}	2.41×10^1	5.00×10^9	4.66×10^0	1.83×10^0	5.36×10^0
223	5.40×10^0	1.94×10^{-1}	3.74×10^1	5.00×10^9	6.69×10^1	3.55×10^0	6.70×10^0
224	5.49×10^0	5.82×10^{-3}	2.02×10^1	5.00×10^9	4.21×10^0	1.81×10^0	5.52×10^0
225	5.59×10^0	3.54×10^{-2}	1.46×10^2	5.00×10^9	1.04×10^1	2.24×10^0	5.79×10^0
226	5.74×10^0	6.02×10^{-2}	9.79×10^1	5.00×10^9	1.58×10^1	2.50×10^0	6.10×10^0
227	5.84×10^0	2.03×10^{-2}	1.26×10^2	5.00×10^9	6.96×10^0	2.08×10^0	5.96×10^0
228	5.85×10^0	7.86×10^{-3}	6.98×10^1	5.00×10^9	4.61×10^0	1.88×10^0	5.89×10^0
229	5.90×10^0	1.49×10^{-2}	4.98×10^1	5.00×10^9	5.88×10^0	2.00×10^0	5.99×10^0
230	5.94×10^0	1.00×10^{-1}	1.73×10^2	5.00×10^9	2.53×10^1	2.88×10^0	6.61×10^0
231	6.17×10^0	5.90×10^{-2}	2.70×10^2	5.00×10^9	1.38×10^1	2.53×10^0	6.56×10^0
232	6.29×10^0	1.12×10^{-1}	2.31×10^2	5.00×10^9	2.54×10^1	3.01×10^0	7.08×10^0
233	6.30×10^0	1.07×10^{-1}	2.18×10^2	5.00×10^9	2.40×10^1	2.97×10^0	7.06×10^0
234	6.41×10^0	1.44×10^{-2}	6.12×10^1	5.00×10^9	5.50×10^0	2.03×10^0	6.51×10^0
235	6.42×10^0	1.19×10^{-2}	1.19×10^2	5.00×10^9	5.15×10^0	2.00×10^0	6.50×10^0
236	6.47×10^0	1.90×10^{-2}	1.65×10^2	5.00×10^9	6.25×10^0	2.11×10^0	6.59×10^0
237	6.47×10^0	3.80×10^{-2}	1.10×10^2	5.00×10^9	9.35×10^0	2.34×10^0	6.73×10^0
238	6.48×10^0	1.62×10^{-1}	6.23×10^2	5.00×10^9	3.63×10^1	3.42×10^0	7.73×10^0
239	6.52×10^0	1.35×10^{-2}	1.37×10^2	5.00×10^9	5.37×10^0	2.03×10^0	6.61×10^0
240	6.52×10^0	1.89×10^{-2}	1.70×10^2	5.00×10^9	6.24×10^0	2.11×10^0	6.65×10^0
241	6.66×10^0	5.01×10^{-2}	3.13×10^2	5.00×10^9	1.09×10^1	2.48×10^0	7.02×10^0
242	6.68×10^0	1.84×10^{-1}	1.28×10^3	5.00×10^9	3.84×10^1	3.60×10^0	8.18×10^0
243	6.79×10^0	8.69×10^{-2}	2.19×10^2	5.00×10^9	1.71×10^1	2.84×10^0	7.44×10^0
244	6.84×10^0	6.82×10^{-2}	1.88×10^2	5.00×10^9	1.37×10^1	2.67×10^0	7.34×10^0
245	6.97×10^0	6.00×10^{-3}	5.62×10^1	5.00×10^9	3.94×10^0	1.92×10^0	7.01×10^0
246	6.98×10^0	6.38×10^{-3}	2.95×10^1	5.00×10^9	4.06×10^0	1.93×10^0	7.03×10^0
247	7.00×10^0	1.00×10^{-3}	6.98×10^1	5.00×10^9	2.81×10^0	1.78×10^0	7.01×10^0
248	7.00×10^0	2.00×10^{-3}	1.99×10^1	5.00×10^9	3.13×10^0	1.82×10^0	7.01×10^0
249	7.00×10^0	5.00×10^{-3}	2.28×10^1	5.00×10^9	3.83×10^0	1.90×10^0	7.04×10^0
250	7.00×10^0	1.00×10^{-2}	1.14×10^2	5.00×10^9	4.65×10^0	2.00×10^0	7.07×10^0
251	7.00×10^0	2.00×10^{-2}	2.09×10^2	5.00×10^9	6.13×10^0	2.16×10^0	7.14×10^0
252	7.00×10^0	5.00×10^{-2}	3.63×10^2	5.00×10^9	1.04×10^1	2.51×10^0	7.37×10^0
253	7.00×10^0	1.00×10^{-1}	2.77×10^2	5.00×10^9	1.86×10^1	2.97×10^0	7.78×10^0
254	7.00×10^0	2.00×10^{-1}	3.88×10^3	5.00×10^9	3.56×10^1	3.75×10^0	8.75×10^0
255	7.00×10^0	5.00×10^{-1}	4.16×10^5	5.00×10^9	2.51×10^1	5.72×10^0	1.40×10^1
256	7.03×10^0	1.59×10^{-1}	5.88×10^2	5.00×10^9	2.95×10^1	3.44×10^0	8.35×10^0
257	7.20×10^0	4.70×10^{-2}	1.73×10^2	5.00×10^9	9.69×10^0	2.49×10^0	7.55×10^0
258	7.22×10^0	1.36×10^{-1}	4.45×10^2	5.00×10^9	2.37×10^1	3.28×10^0	8.36×10^0
259	7.32×10^0	8.88×10^{-2}	6.26×10^2	5.00×10^9	1.54×10^1	2.90×10^0	8.04×10^0
260	7.52×10^0	6.13×10^{-3}	3.18×10^1	5.00×10^9	3.96×10^0	1.96×10^0	7.56×10^0
261	7.62×10^0	2.01×10^{-2}	2.65×10^2	5.00×10^9	5.80×10^0	2.20×10^0	7.77×10^0
262	7.62×10^0	6.15×10^{-2}	5.44×10^2	5.00×10^9	1.10×10^1	2.67×10^0	8.12×10^0
263	7.65×10^0	5.29×10^{-2}	4.91×10^2	5.00×10^9	9.84×10^0	2.58×10^0	8.08×10^0
264	7.65×10^0	1.08×10^{-1}	8.23×10^2	5.00×10^9	1.71×10^1	3.09×10^0	8.57×10^0
265	7.66×10^0	1.08×10^{-2}	6.16×10^1	5.00×10^9	4.62×10^0	2.06×10^0	7.74×10^0
266	7.67×10^0	1.38×10^{-1}	9.57×10^2	5.00×10^9	2.15×10^1	3.34×10^0	8.90×10^0
267	7.81×10^0	7.14×10^{-3}	3.95×10^1	5.00×10^9	4.08×10^0	2.00×10^0	7.87×10^0
268	7.96×10^0	4.90×10^{-2}	2.39×10^2	5.00×10^9	9.08×10^0	2.57×10^0	8.37×10^0
269	8.04×10^0	5.93×10^{-3}	7.57×10^1	5.00×10^9	3.85×10^0	1.99×10^0	8.09×10^0
270	8.08×10^0	7.17×10^{-2}	3.25×10^2	5.00×10^9	1.15×10^1	2.80×10^0	8.70×10^0
271	8.11×10^0	5.08×10^{-2}	5.77×10^2	5.00×10^9	9.12×10^0	2.60×10^0	8.55×10^0
272	8.31×10^0	5.71×10^{-2}	6.63×10^2	5.00×10^9	9.61×10^0	2.67×10^0	8.81×10^0
273	8.37×10^0	4.85×10^{-2}	2.77×10^2	5.00×10^9	8.66×10^0	2.59×10^0	8.79×10^0
							Continued on next page

ID	M_{core} [$M_\oplus$]	f [-]	Age (t = 0) [yr]	Age (t = t_{final}) [yr]	$R_P(t = 0)$ [$R_\oplus$]	$R_P(t$ = t_{final}) [$R_\oplus$]	M_P [$M_\oplus$]
274	8.56×10^0	8.53×10^{-3}	1.20×10^2	5.00×10^9	4.15×10^0	2.07×10^0	8.63×10^0
275	8.63×10^0	3.93×10^{-2}	2.59×10^2	5.00×10^9	7.50×10^0	2.50×10^0	8.98×10^0
276	8.66×10^0	1.20×10^{-1}	6.44×10^2	5.00×10^9	1.59×10^1	3.27×10^0	9.85×10^0
277	8.74×10^0	7.96×10^{-2}	9.83×10^2	5.00×10^9	1.14×10^1	2.92×10^0	9.49×10^0
278	8.92×10^0	5.96×10^{-2}	3.78×10^2	5.00×10^9	9.29×10^0	2.74×10^0	9.49×10^0
279	8.95×10^0	1.67×10^{-1}	1.93×10^3	5.00×10^9	1.96×10^1	3.66×10^0	1.07×10^1
280	9.03×10^0	2.84×10^{-2}	5.20×10^2	5.00×10^9	6.22×10^0	2.40×10^0	9.29×10^0
281	9.05×10^0	8.51×10^{-3}	6.17×10^1	5.00×10^9	4.10×10^0	2.10×10^0	9.13×10^0
282	9.38×10^0	7.94×10^{-2}	1.21×10^3	5.00×10^9	1.06×10^1	2.96×10^0	1.02×10^1
283	9.42×10^0	9.93×10^{-2}	6.74×10^2	5.00×10^9	1.23×10^1	3.14×10^0	1.05×10^1
284	9.50×10^0	4.16×10^{-2}	3.54×10^2	5.00×10^9	7.25×10^0	2.58×10^0	9.91×10^0
285	9.50×10^0	8.98×10^{-3}	1.54×10^2	5.00×10^9	4.10×10^0	2.13×10^0	9.59×10^0
286	9.54×10^0	4.40×10^{-2}	8.14×10^2	5.00×10^9	7.39×10^0	2.61×10^0	9.98×10^0
287	9.61×10^0	1.84×10^{-2}	3.46×10^2	5.00×10^9	5.07×10^0	2.30×10^0	9.79×10^0
288	9.63×10^0	1.29×10^{-1}	9.44×10^2	5.00×10^9	1.46×10^1	3.41×10^0	1.11×10^1
289	9.71×10^0	2.05×10^{-2}	1.82×10^2	5.00×10^9	5.26×10^0	2.33×10^0	9.91×10^0
290	9.71×10^0	4.53×10^{-2}	3.92×10^2	5.00×10^9	7.48×10^0	2.63×10^0	1.02×10^1
291	9.74×10^0	3.18×10^{-2}	3.08×10^2	5.00×10^9	6.28×10^0	2.48×10^0	1.01×10^1
292	9.82×10^0	5.50×10^{-2}	4.71×10^2	5.00×10^9	8.20×10^0	2.75×10^0	1.04×10^1
293	9.87×10^0	3.92×10^{-2}	3.73×10^2	5.00×10^9	6.87×10^0	2.58×10^0	1.03×10^1